ADVANCED MATERIALS
www.advmat.de

Beyond Conventional Carbon Activation: Creating Porosity without Etching Using Cesium Effect

Jiaxin Li, Yaolin Xu, Pengzhou Li, Antje Völkel, Fernando Igoa Saldaña, Markus Antonietti, Nieves López-Salas, and Mateusz Odziomek**

Facile synthesis of porous carbon with high yield and high specific surface area (SSA) from low-cost molecular precursors offers promising opportunities for their industrial applications. However, conventional activation methods using potassium and sodium hydroxides or carbonates suffer from low yields (<20%) and poor control over porosity and composition especially when high SSAs are targeted (>2000 m^2 g^{-1}) because nanopores are typically created by etching. Herein, a non-etching activation strategy is demonstrated using cesium salts of low-cost carboxylic acids as the sole precursor in producing porous carbons with yields of up to 25% and SSAs reaching 3008 m^2 g^{-1}. The pore size and oxygen content can be adjusted by tuning the synthesis temperature or changing the molecular precursor. Mechanistic investigation unravels the non-classical role of cesium as an activating agent. The cesium compounds that form in situ, including carbonates, oxides, and metallic cesium, have extremely low work function enabling electron injection into organic/carbonaceous framework, promoting condensation, and intercalation of cesium ions into graphitic stacks forming slit pores. The resulting porous carbons deliver a high capacity of 252 mAh g^{-1} (567 F g^{-1}) and durability of 100 000 cycles as cathodes of Zn-ion capacitors, showing their potential for electrochemical energy storage.

1. Introduction

Porous carbons are essential for diverse applications, especially for sorption, energy conversion, and energy storage, owing to their high specific surface area (SSA), tunable porosity and surface chemistry, and high stability.[1] The synthesis of porous carbon through carbonization of organics, followed by an activation process, is regarded as a versatile strategy in both academia and industry.[2] Nonetheless, it remains challenging to simultaneously achieve high carbon yield (>20%), high SSA (>2000 m^2 g^{-1}), and controlling pore size and composition, when starting from molecular precursors.[3] To access highly porous carbon, activation agents such as alkali metal (K and Na) based hydroxides, carbonates, and bicarbonates have been extensively employed and their effects in creating porosity have been well studied.[4] However, cesium (Cs), a heavier member of the alkali metal group, has been rather omitted in carbon research despite its distinct properties that influence the condensation of organics and the activation process of carbon.[5] Compared to other alkali metal compounds (K and Na), Cs compounds have lower melting points (Table S1, Supporting Information), higher basicity, and stronger interaction with carbon.[6] Notably, Cs oxides, especially suboxides,[7] are recognized for their low work function, and finding application as electron injection layers in solar cells to enhance power conversion efficiency.[8]

J. Li, A. Völkel, M. Antonietti, N. López-Salas[+], M. Odziomek
Colloid Chemistry Department
Max Planck Institute of Colloids and Interfaces
Am Mühlenberg 1, 14476 Potsdam, Germany
E-mail: nieves.lopez.salas@uni-paderborn.de; mateusz.odziomek@mpikg.mpg.de

The ORCID identification number(s) for the author(s) of this article can be found under https://doi.org/10.1002/adma.202311655

[+]Present address: Department of Chemistry, Paderborn University, Warburger Straße 100, 33098 Paderborn, Germany

DOI: 10.1002/adma.202311655

Y. Xu
Institute of Electrochemical Energy Storage
Helmholtz-Zentrum Berlin für Materialien und Energie
14109 Berlin, Germany

P. Li
State Key Laboratory of Molecular Engineering of Polymers, Department of Macromolecular Science, and Laboratory of Advanced Materials
Fudan University
Shanghai 200438, China

F. I. Saldaña
Deutsches Elektronen-Synchrotron DESY
Notkestraße 85, 22607 Hamburg, Germany

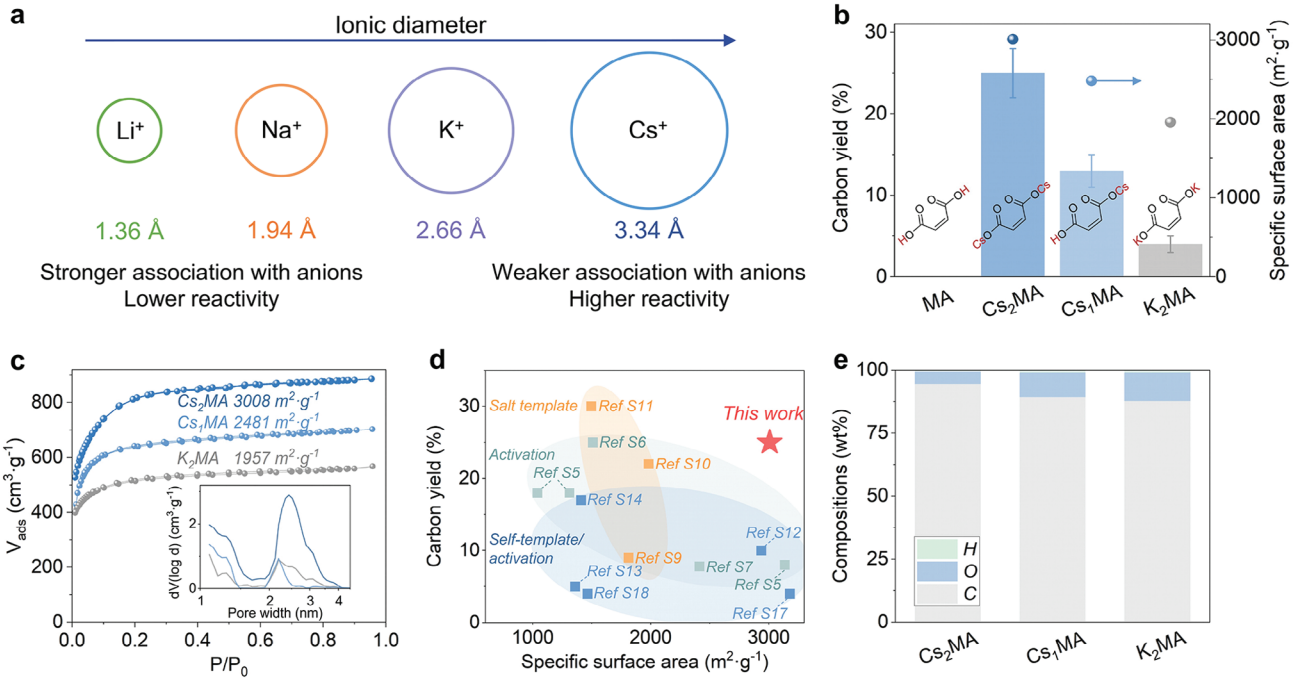

Figure 1. Impact of Cs ions on the synthesis of porous carbons. a) Schematic illustrating the influence of ionic sizes of alkali ions on their association degree with anions and reactivity. b) Carbon yields and SSAs, and c) N_2 sorption isotherms at 77 K (inset: pore size distributions) of porous carbons obtained from Cs_2MA, Cs_1MA, and K_2MA as the precursors. d) Comparison of yields and SSAs of porous carbons derived from Cs_2MA and other synthetic strategies starting from molecular precursors (see citations in Supporting Information). e) Elemental compositions of porous carbons obtained from Cs_2MA, Cs_1MA, and K_2MA.

Cs salts have also received significant attention as (co)catalysts in organic synthesis leading to higher yields, lower synthesis temperatures, and exceptional selectivity compared with other alkali metal salts.[9] The term "cesium effect" has been coined to describe the role and effectiveness of Cs salts in catalytic processes. For instance, Cs salts, such as Cs_2CO_3 and cesium acetate, catalyze various reactions like C—H activation, C—C coupling, and macro-cyclization.[9,10] All these reactions are involved in the thermal condensation of molecular precursors to form carbonaceous materials. Although the exact mechanisms behind this effect are not yet fully understood, it is believed that the larger size of Cs ion than other alkali ions plays a significant role (**Figure 1a**, Table S1, Supporting Information). The larger size of Cs ion leads to weaker association with anions in the reaction medium, enhancing their reactivity. Further, Cs ions can effectively interact with oxygen-containing functional groups in organic compounds, promoting the elimination of these functional groups and the formation of covalent networks.[9,11] For example, Cs ions effectively catalyze dehydration and decarboxylation accelerating condensation reactions,[12] and activate carbonyl groups generating enolate anions, thus facilitating reactions such as substitution, addition, or macrocyclization.[9,13]

Furthermore, the activation process involving Cs can occur at notably lower temperatures (≈600 °C) than K or Na compounds (>800 °C), due to lower melting points and decomposition temperatures of Cs compounds. Consequently, Cs oxides and metal can be generated at much lower temperatures and serve as powerful activating agents. Importantly, metallic Cs interact strongly with carbons and intercalate into graphitic layers more efficiently than K, Na, and Li.[6] We have recently shown that by heating solely cesium acetate between 500 and 800 °C, Cs ions can effectively catalyze the condensation of acetate groups, resulting in porous carbon with an SSA of up to 2936 $m^2\ g^{-1}$ and yield of 10% at 800 °C.[14]

Building upon this finding, we have extended this method to other low-cost carboxylic acids, enhancing carbon yields up to 25% while maintaining a comparable SSA of 3008 $m^2\ g^{-1}$. For that, dicesium maleate (Cs_2MA) is employed as a model self-templating precursor, which can be further simplified to a mixture of commercially available Cs_2CO_3 and maleic acid (MA). Interestingly, by slightly modifying the carboxylic acid molecule, the pore size distribution can be effectively tuned in a narrow range giving access to molecularly designed carbons. Detailed analysis of the carbons synthesized at varying temperatures indicates that the active Cs species (oxides, metal) form at temperatures over 200 °C lower than other alkali metals, profoundly influencing the activation process. Contrary to the conventional activation process, we did not observe the oxidation of carbon atoms and the etching process that leads to micropore creation. Instead, Cs intercalation has been identified as the primary driver behind the significant surge in SSA and pore volume. Due to the reduced temperatures required for the thermal condensation and activation of carbonaceous networks, a significant fraction of oxygen (16.4–13.5 wt%) could stay integrated into the carbon structures. The resultant carbon materials present promise as cathodes for aqueous Zn-ion and aprotic Na-ion capacitors with exceptional capacity and stability.

Table 1. Compositions and porosities of condensed products obtained at different conditions.

T [°C]	Precursor	Salt	C[a] [wt%]	H[a] [wt%]	O[a] [wt%]	Cs[b] [wt%]	SSA[c] [m^2 g^{-1}]	V_{Micro}[d] [cm^3 g^{-1}]	V_{Meso}[d] [cm^3 g^{-1}]	CO_2 uptake[e] [mmol g^{-1}]	Yield[f] [%]
800	Cs_2MA	–	92.9	0.6	4.8	0.3	3008	0.84	0.32	–	25
	Cs_1MA	–	88.5	1.1	9.4	0.1	2481	0.70	0.24	–	13
	K_2MA	–	87.7	1.1	11.2	–	1957	0.64	0.17	–	4
450	MA	Cs_2CO_3	83.6	3.0	16.4	0.1	891	0.30	0.10	4.0	28
500			85.0	3.7	15.1	0.1	1410	0.50	0.07	6.1	27
600			82.8	1.7	13.5	0.1	1988	0.72	0.05	9.0	26
700			87.1	1.5	11.5	0.1	2351	0.83	0.05	8.3	24
800			93.9	0.4	4.3	0.1	3066	0.88	0.38	8.1	22
800	Fumaric acid	Cs_2CO_3	92.9	0.5	5.2	0.1	2880	0.82	0.36	6.7	22
	Succinic acid		87.9	1.0	4.5	0.1	2710	0.67	0.64	5.7	10
	Acrylic acid		93.1	0.5	6.4	0.1	2604	0.88	0.12	9.8	18

[a] C, H, and O content from the elemental combustion analysis; [b] Metal content from the inductively coupled plasma atomic emission spectroscopy. Since the content of C, H, O, and Cs was measured using different methods, the mass ratio sum of all the above elements may not always equal 100%; [c] SSAs were evaluated in P/P_0 from 0.05 to 0.25 based on the BET equation; [d] The pore size distributions were calculated from the N_2 adsorption and desorption isotherms at 77 K using the quenched solid density functional theory method; [e] CO_2 uptake was obtained at 273 K and 100 kPa; [f] The carbon yield was determined by comparing the final material mass to either the initial carbon precursor mass or the mass of the organic species in Cs_2MA, Cs_1MA, or K_2MA.

2. Results and Discussion

2.1. Thermal Condensation of MA versus Cs_2MA and K_2MA

MA serves as a model molecular precursor as it is easily obtained from biomass at a low cost.[15] With four sp^2 carbon atoms and a C═C bond, MA can support the formation of polymeric and, subsequently, carbonaceous networks. However, direct pyrolysis of MA at atmospheric pressure did not yield any material, as MA sublimated, evaporated, or decomposed to gaseous products around 137 °C (Figure S1, Supporting Information).[16] In contrast, the dicesium salt of MA, denoted as Cs_2MA (CsOOC—CH═CH—COOCs), yields porous carbon with a yield of 25% and an SSA of 3008 m^2 g^{-1} upon condensation at 800 °C (Figure 1b,c and **Table 1**), surpassing other methods as depicted in Figure 1d and listed in Table S2, Supporting Information. Simultaneously achieving high yield and large SSA from molecular precursors is rare, primarily because nanopores typically form at the expense of carbon atoms in conventional activation processes based on etching.[3a,17] For comparison, the use of a monosalt precursor (HOOC—CH═CH—COOCs, Cs_1MA) leads to a yield of 13% and an SSA of 2481 m^2 g^{-1}, while the dipotassium salt (K_2MA) only gives a 4% yield and an SSA of 1957 m^2 g^{-1}. The Cs_2MA-derived sample contains 92.9 wt% carbon and 4.8 wt% oxygen while it is 87.7 wt% carbon and 11.2 wt% oxygen for the one derived from K_2MA (KOOC—CH═CH—COOK) (Figure 1e). The significant differences between Cs and K salts emphasize the impact of Cs on framework formation and pore development.

Nevertheless, cesium maleate is not a commercial product and needs to be synthesized. To further simplify the process for non-chemists, we harness the acidic properties of carboxylic acids. MA is a stronger acid (pKa1 of 1.9 and pKa2 of 6.1) than carbonic acid (pKa1 of 6.8 and pKa2 of 9.9) (Table S3, Supporting Information). Mixing MA with Cs_2CO_3 leads to a typical exchange reaction between a stronger acid and the salt of a weaker acid, forming the salt of a strong acid (Cs_2MA) and a weak acid (H_2CO_3). This reaction occurs at 100–200 °C (to be discussed later), and the formed H_2CO_3 immediately decomposes into H_2O and CO_2 leaving the reaction. Therefore, in a subsequent study, MA and Cs_2CO_3 were mixed in a mass ratio of 1:10 (equivalent to a molar ratio of 1:3.6 ensuring complete conversion of MA), heated between 450 and 800 °C, washed and dried to obtain the resulting products (see detailed experimental procedures in the Supporting Information). The products were labeled as MC-T, where T denotes the condensation temperature.

2.2. The Structure and Microstructure of Cs_2MA-Derived Carbons

The resulting carbonaceous materials were obtained with notably higher yields (28–22%) compared to the previously reported porous carbons obtained from molecular precursors (**Figure 2a** and Table S2, Supporting Information). Scanning electron microscopic images show smooth scaffolds with 1–5 µm cavities, presumably occupied by excessive Cs_2CO_3 before decomposition/washing (Figure S2, Supporting Information). Elemental combustion analyses revealed a significant decrease in oxygen content from 16.4 to 4.3 wt% and hydrogen from 3.0 to 0.4 wt% between MC450 and MC800 (Figure 2a and Table 1), which aligns well with the reduction in the reaction yield. The products obtained between 450 and 600 °C reveal a high oxygen content of 16.4–13.5 wt%. The amount of Cs is below 0.1 wt% for all products according to the results of inductively coupled plasma atomic emission measurements. The Fourier-transformed infrared (FT-IR) spectrum of MC450 (Figure 2b) displays signals corresponding to C═O at 1690 cm^{-1}, C═C at 1560 cm^{-1}, and a broad band spanning 1300–950 cm^{-1} ascribed to C—O groups, pointing at the

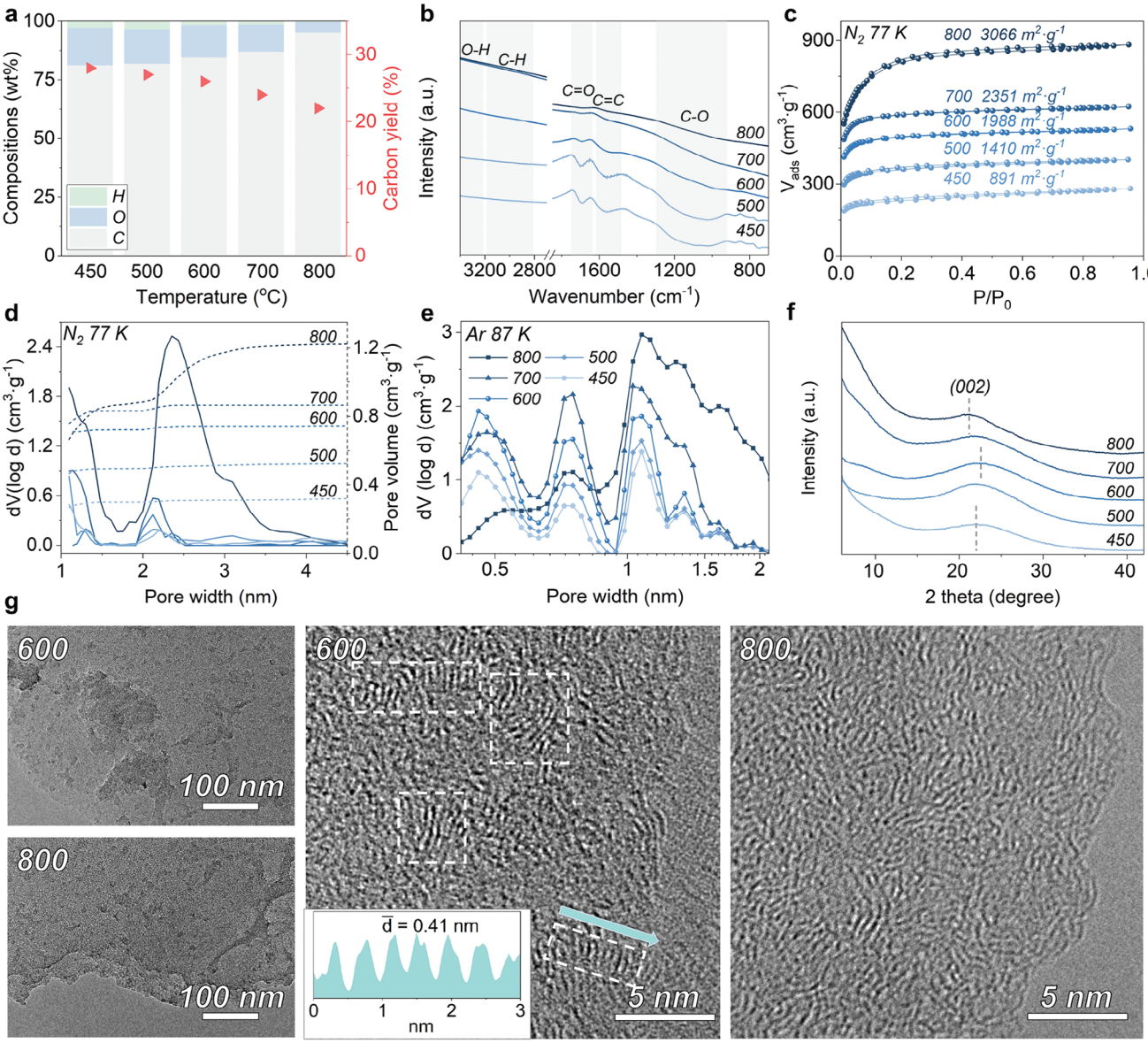

Figure 2. Structural properties of the porous carbons obtained from MA and Cs_2CO_3 between 450 and 800 °C. a) Elemental compositions and carbon yields, b) FT-IR spectra, c) N_2 sorption isotherms at 77 K, d) pore size distributions and cumulative pore volumes calculated from N_2 sorption isotherms, e) micropore size distributions calculated from the Ar sorption isotherms at 87 K, f) XRD patterns, and g) TEM and high-resolution TEM images.

formation of a carbon-oxygen framework. Importantly, the spectrum of MC450 is flat between 3300 and 2700 cm^{-1}, the region related to C—H and O—H bonds. This implies a highly conjugated character of the carbon framework, which is unusual for a temperature as low as 450 °C. At higher temperatures, the intensity of the bands between 1700 and 900 cm^{-1} gradually weakens and eventually disappears at 800 °C, as a result of proceeding carbon condensation with simultaneous removal of heteroatoms.

N_2 sorption measurements were performed at 77 K to investigate the pore structure of the carbonaceous products (Figure 2c). The samples feature Type I(b) isotherms with a strong N_2 uptake at low relative pressures ($P/P_0 < 0.1$), typical for micropores, and a plateau above $P/P_0 = 0.2$.[18] The calculated Brunauer–Emmett–Teller (BET) SSA and micropore volume of samples between 450 and 800 °C increases from 891 to 3066 $m^2\ g^{-1}$ and from 0.30 to 0.88 $cm^3\ g^{-1}$, respectively. The pore size distributions are depicted in Figure 2d and summarized in Table 1. While the samples between 450 and 700 °C show almost only microporosity (pore width < 2 nm), MC800 contains a second population of pores with sizes at 2–4 nm. Argon (Ar) sorption measurements at 87 K with high resolution at low partial pressures ($P/P_0 \approx 10^{-6}$) were conducted to assess the micropore size distributions of the products (Figure S3, Supporting Information). Between 450 and 700 °C, the products exhibit an increase in ultramicropores (pore width < 0.8 nm) (**Figure 3e**). At 800 °C, the ultramicropore volume decreases, and the volume of larger micropores (pore width > 1 nm) increases, possibly due to ultramicropore merging or expansion.

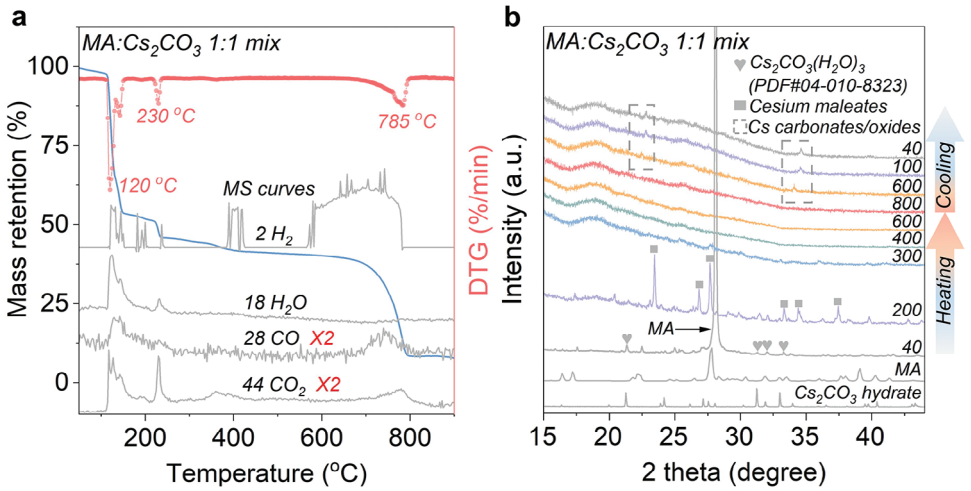

Figure 3. Synthetic mechanism analyses of Cs-mediated porous carbons. a) TGA-MS curves under helium and b) in situ XRD patterns of the 1:1 mass ratio mixture of MA and Cs_2CO_3 under N_2. XRD patterns of Cs_2CO_3 and MA were provided for reference. Cs_2CO_3 readily absorbs moisture from the air and instantly converts it into its hydrate when exposed to the air.

Besides, the samples show an increase in CO_2 uptake at 273 K from 450 to 600 °C reaching 9.0 mmol g^{-1} of CO_2 adsorbed (Figure S4, Supporting Information). At higher temperatures, the CO_2 uptake slightly decreases to 8.1 mmol g^{-1} for MC800 (all data are summarized in Table 1). These values are competitive to the state-of-the-art CO_2 adsorbents,[19] highlighting the potential of Cs-mediated porous carbons in CO_2 adsorption or further catalytic conversion.[20] Such high uptakes originate primarily from very high micropore volumes, especially ultramicropores (pore width < 0.8 nm) which favor strong interactions between CO_2 molecules and two neighboring pore walls.[21] Besides, the electron-rich oxygen sites can interact with electron-deficient carbon atoms in CO_2 molecules, promoting CO_2 adsorption by Lewis acid-base interaction.[22] Therefore, MC600 shows the highest CO_2 uptake, due to its highest ultramicropore volume and maintained high oxygen content of 13.5 wt%.

The evolution of the structure as a function of condensation temperature was studied by X-ray diffraction (XRD), Raman spectroscopy, and high-resolution transmission electron microscopy (HR-TEM). The XRD patterns, depicted in Figure 2f, present broad and low-intensity (002) diffraction peaks, typical for turbostratic carbonaceous structures. The (002) peak of MC450 is centered at 22.1°, and for MC600 it slightly shifts to a higher angle of 22.5° and returns to a lower angle (21.1°) for MC800. This indicates that the structure becomes first more compact to open back again at 800 °C. The large intensity increase of low-angle scattering (below 10°) for samples treated at 700 and 800 °C is characteristic of microporous materials with high SSAs.[23] The Raman spectra exhibit two broad bands typically denoted as D (breathing mode of sp2 carbon atoms in aromatic rings at defect sites) and G bands (C=C bonds) (Figure S5, Supporting Information). While there is no clear difference in the shape or intensity of D and G bands, the D band significantly shifts to lower wavenumbers from 1346 cm^{-1} for MC450 to 1330 cm^{-1} for MC600, followed by a shift back to 1348 cm^{-1} for MC800. Schuepfer et al. showed that the position of D band is a good indicator of the lateral size of conjugated domains in disordered carbons.[24] This trend aligns with XRD findings that MC600 has the most compact and ordered structure. TEM images of MC600 and MC800 reveal macroscopically homogeneous layers (Figure 2g), corresponding to the cavity walls observed in the scanning electron microscopy images (Figure S2, Supporting Information). The HR-TEM of MC600 reveals a combination of disordered sp2 carbon fringes and short but locally organized stacked graphitic layers that take random orientations to each other. The interlayer spacing is measured between 0.37 and 0.41 nm, in agreement with that calculated value from XRD analysis (0.39 nm). HR-TEM image of MC800 shows a more disordered structure with less pronounced local stacking, consistent with the XRD and Raman analysis.

2.3. Thermal Transformation of Cs_2MA and Cs_2CO_3

To get further insights into the mechanism of the process and the structural rearrangements occurring, the thermogravimetric analysis coupled with mass spectroscopy (TGA-MS) and in situ XRD were performed. MA: Cs_2CO_3 mixtures of 1:1 (Figure 3a,b) and 1:10 (Figures S6 and S7, Supporting Information) mass ratios were used to decouple the signals from in situ formed Cs maleate and bulk Cs_2CO_3. The TGA-MS curves of a 1:1 mixture (Figure 3a) show a mass loss of 44% between 115 and 150 °C, accompanied by the release of CO_2, CO, H_2O, and H_2. This is the overlapping decomposition of carbonic acid and the sublimation/decomposition of MA excess. Further mass loss at 230 °C with the generation of CO_2, H_2O, and H_2 indicates the onset of the decomposition of cesium maleate and condensation of organics, which continues up to 400 °C. At this stage, the evolution of CO_2 and H_2 occurs as a result of condensation and aromatization reactions. Notably, the most severe aromatization starts at about 570 °C and continues to about 785 °C with strong H_2 evolution. It is important to note that the mass loss from the carbon network at this temperature range is minimal, as indicated by the TGA, differential thermal gravimetry curve, and the calculated yields.

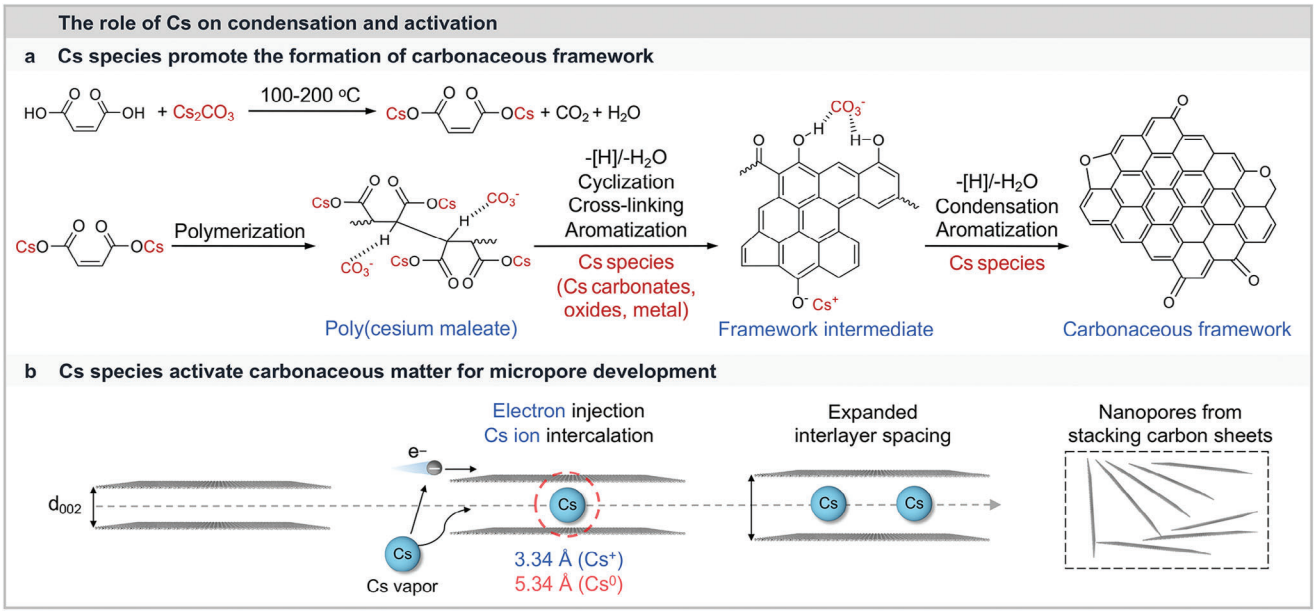

Figure 4. Proposed effects of Cs on condensation and activation. a) The role of Cs in promoting the formation of the carbonaceous framework. b) The role of Cs as an electron injection and intercalation agent for the creation of nanopores. The diameter of Cs atom and ion are marked in the scheme.

At around 700 °C, the strong mass loss is related to the evaporation of Cs species as discussed further in the manuscript.

A similar TGA-MS pattern is observed for the 1:10 mixture (Figure S6, Supporting Information). However, the peaks corresponding to the evolution of carbon species are hidden due to the large excess of Cs_2CO_3. The onset of the most intense mass loss (about 77% in total) is at about 530 °C, which corresponds to the beginning of Cs_2CO_3 decomposition to Cs_2O and CO_2. Theoretically, the released CO_2 should only account for 13.5% of the mass of Cs_2CO_3, much lower than the real mass loss, which suggests that the in situ generated Cs_2O is not stable at this temperature. Cs_2O has been reported to undergo complex disproportionation reactions generating Cs_2O_2, CsO_2, and Cs metal.[25] Therefore, the sharp mass loss is attributed to the evaporation of Cs oxides and metal (boiling point: 671 °C) within the helium flow. The notable difference in the temperature onset of mass loss for Cs species evaporation between 1:1 (≈670 °C) and 1:10 (≈530 °C) ratio samples suggests that Cs_2MA might not decompose into carbonate but into other Cs species like Cs oxides, suboxides, and metal. These formed Cs species could potentially be stabilized within the carbon networks, as intercalated compounds, especially given these related Cs species have much lower boiling points.

In situ XRD patterns of the 1:1 mixture reveal the formation of Cs maleates at 200 °C (Figure 3b and Figure S8, Supporting Information) with the disappearance of peaks related to MA and Cs_2CO_3. The decomposition of Cs maleate at 300 °C is signaled by the disappearance of the diffraction peaks. In the meantime, no crystalline phase of Cs is formed which might indicate the formed poorly crystalline phases are homogenously distributed within the formed carbonaceous network. There is a possibility that the formed oxide or metallic phase is molten as these are low melting point phases. Notably, no XRD peak is observed from 400 to 800 °C. The broad hump at around 18° is to be attributed to the Kapton window of the high-temperature chamber (Figure S9, Supporting Information). During the cooling stage, several new peaks appear below 600 °C owing to the recrystallization of Cs oxides or carbonates. However, we could not unambiguously assign them due to the rich structural complexity of Cs oxides and carbonates. In the case of the in situ XRD experiment with a 1:10 mixture (Figure S7, Supporting Information), we can follow the transformation of bulk Cs_2CO_3 as its scattering cross-section is orders of magnitude higher than that of carbon. The peaks from crystalline Cs_2CO_3 remain visible up to 700 °C, with a slight shift to lower angles due to the thermal expansion of the unit cell at high temperatures. At 800 °C, no peak is observed due to Cs_2CO_3 melting and decomposition. Similar to the 1:1 mixture, the appearance of new peaks during cooling below 500 °C is attributed to the recrystallization of Cs oxides or residual carbonates during cooling.

2.4. The Effect of Cs on Condensation and Activation

Based on the analysis above, we can summarize the effect of Cs on the formation of a porous carbonaceous framework. Initially, around 130 °C, MA melts and reacts with Cs_2CO_3, forming cesium maleates (**Figure 4a**). As the temperature rises above 200 °C, cesium maleates undergo complex polymerization, decomposition, cyclization, cross-linking, and concomitant aromatization reactions, which leads to the formation of a continuous oxocarbon framework at temperatures as low as 400 °C. In the beginning, the oligomeric species of poly(cesium maleate) form due to the presence of a double bond within the MA molecule, which is confirmed by the matrix-assisted laser desorption/ionization time of flight analysis (Figure S10, Supporting Information). Notably, at 400 °C, the carbon framework is already highly conjugated as FT-IR analysis did not detect C—H and O—H groups.

This supports the catalytic effect of Cs ions on condensation, especially given that using K, Na, and Li does not yield the same effect (Figures S11 and S12, Supporting Information).

Grasping the exact fate of Cs is difficult because Cs oxides and metal are highly reactive and have low melting points. During the condensation/crosslinking of the carbon network, Cs are homogeneously distributed as counter ions to oxygen functionalities and successively transformed into a mixture of poorly crystallized oxides, as typically happens to carboxylic salts.[26] Cs oxides are chemically not well-defined and undergo complex disproportionation reactions forming suboxides (e.g., Cs_7O, Cs_4O, Cs_3O, and Cs_7O_2)[25,27] and even metallic Cs.[28] It is worth noting that such basic oxides easily capture CO_2-forming carbonates. All these Cs species are efficient electron-injection agents,[29] for instance, used in organic electronic devices due to their low work function.[8] In fact, it has been shown that oxidized Cs clusters have one of the lowest work function, especially for Cs suboxides.[30] The layers of Cs oxides are deposited on different materials to decrease their work function.[7] Therefore, we speculate that, at elevated temperatures, Cs oxides are able to act as electron donors triggering faster polymerization, condensation reactions, and the aromatization of covalent networks. Meantime, the in situ formed clusters of Cs species serve as templates for creating the initial porosity.

Up to 600 °C, the carbon structure experiences further decomposition of oxygen functionalities and undergoes aromatization reactions, which include H_2 evolution. This process results in the formation of new pores (templated by Cs species) and graphitic domains, as evidenced by HR-TEM and XRD analyses. Beyond 600 °C, we observe a notable transformation: the graphitic domains diminish, and there is a shift in pore size distribution, with an increase in pores larger than 1 nm at the expense of smaller pores (pore width < 1 nm). We attribute this transformation to an intercalation mechanism.

As the temperature rises, Cs oxides/carbonates become more prone to form metallic species or suboxides. These Cs species have a remarkably high affinity for carbon, readily forming intercalation compounds such as CsC_8 and CsC_6. Notably, the formation energy of Cs intercalation compounds is significantly lower compared to other alkali metals, as documented in the literature.[6,31] These Cs species are capable of electron donation, inducing a negative charge on the carbonaceous layers and thereby causing repulsion between these layers. This effect increases the interlayer distance, facilitating the diffusion of Cs cations, which are sizably akin to the spacing in graphitic structures, as shown in Figure 4b. Additionally, it is plausible that similar intercalation compounds may form through the interaction of Cs oxides with carbon.

Furthermore, at temperatures exceeding 500–600 °C, there is a significant decomposition of carbonates into CO_2 and chemically undefined Cs oxides and suboxides,[7] which subsequently disproportionate into metallic Cs.[28b] This process is corroborated by the pronounced mass loss of 77% observed in the TGA of a 1:10 mixture (attributed to evaporation of metallic Cs), as presented in Figure S6, Supporting Information.

The interlayer distances reported for Cs graphitic intercalation compounds typically range from 0.59 to 0.61 nm,[32] which are significantly larger than the interlayer spacing in MC600 (0.37–0.41 nm) determined by HR-TEM and the smallest fraction of ultramicropores (≈ 0.46 nm) identified by Argon sorption. At 800 °C, the emergence of larger pores (pore width > 1 nm) at the expense of the smallest ones might serve as additional evidence of Cs intercalation. Besides, this micropore expansion could also be a result of the merging of the smallest pores, potentially occurring during the release of gases like CO or CO_2, especially considering the high oxygen loss from 11.5 wt% to 4.3 wt% between 700 and 800 °C.

This electron injection and ion intercalation mechanism gain support from the discovery that Cs intercalation graphitic compounds exhibit much higher electron density and in-plane electrical conductivity compared with pristine graphite.[33] Inspiringly, Zhu et al. recent study reveals that α-Li_3N significantly lowers the phase change temperature of graphite to 350 °C due to electron injection from α-Li_3N into graphite.[34] This electron injection expands the interlayer spacing of graphite through increased Columbic repulsion among π electrons within graphitic layers. Similar effects on promoting graphite phase transition were also observed with alkali metals like Li, Na, and K. These observed effects are primarily related to the low work function of Li_3N, Li, Na, and K.[35] Interestingly, Cs species possess even lower work function,[36] further supporting our proposal on electron injection and ion intercalation.

The alkali metal intercalation mechanism has been already described for K. In the case of K, the presence of metallic K is postulated to occur by carbothermal reduction, that is, it is coupled to C═O and CO_2 formation while the metallic K evaporates at temperatures above 800 °C.[37] In comparison, in the case of Cs, the process starts much earlier because the decomposition of Cs_2CO_3, forming Cs oxides and metal, occurs at a temperature over 200 °C lower than that required for K (Figure S13, Supporting Information).[38] At the same time, the formation of Cs suboxides may greatly facilitate electron transfer as well as the ion intercalation process. Besides, Cs atoms, being much bigger than K atoms, bring larger distortion into the carbon networks, leading to higher SSAs. This is exactly what we observed in the samples prepared between 600 and 800 °C (Figures S14 and S15, Table S4, Supporting Information).

Importantly, the conventional activation process is inherently linked with chemical etching, that is, the liberated gaseous carbon oxides take away significant amounts of carbon atoms. However, in our study, the reaction yields at temperatures of 450 and 800 °C are found to be 28% and 22%, respectively, with oxygen content measured at 16.4 wt% and 4.3 wt%. This suggests that the mass loss from 28% to 22% can be mainly attributed to the liberation of CO_2 and CO from the established carbonaceous networks. This phenomenon is consistent with the thermal decomposition of oxygen-containing groups in carbonaceous materials[39] and occurs irrespective of the presence of activating or templating agents. To further prove that, MC450 was reheated at 800 °C in an N_2 atmosphere. The treatment yielded carbon with 70% of the initial mass, resulting in an overall yield of 20% (similar to or a bit lower than MC800). The SSA increases only to 1397 $m^2\ g^{-1}$ after thermal treatment, much lower than that of MC800 (3066 $m^2\ g^{-1}$) (Figure S16, Supporting Information). This shows that Cs activation affects the porosity but not the yield. Consequently, it can be inferred from the present study that Cs species do not engage in the conventional chemical etching of carbon structures,

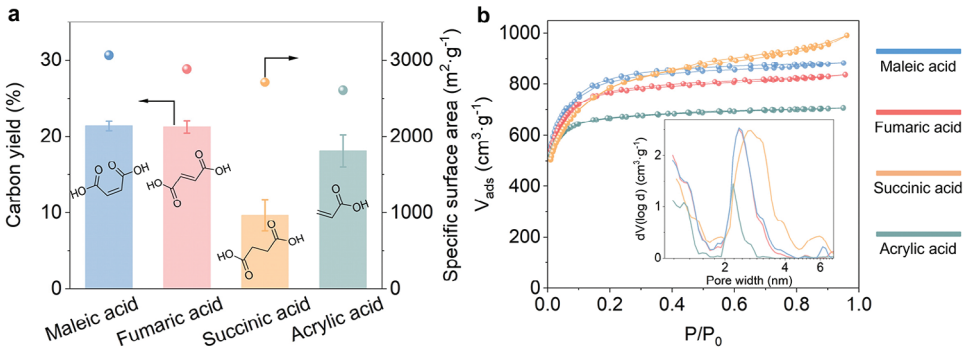

Figure 5. a) Carbon yields, SSAs, and b) N_2 sorption isotherms at 77 K of porous carbons obtained from MA, fumaric acid, succinic acid, or acrylic acid as molecular precursors with Cs_2CO_3 at 800 °C. Inset: pore size distributions.

as is commonly observed with traditional activating agents such as KOH, NaOH, CO_2, or steam.[17]

2.5. Molecular Design of Porous Carbons

Molecular engineering has a major impact on the yields and the structural properties of the materials obtained through bottom-up synthesis. To show that, we compared the yields, chemical compositions, and the pore structures of products obtained from thermal condensation of fumaric acid, succinic acid, and acrylic acid in the presence of Cs_2CO_3 at 800 °C (Table 1). Despite fumaric acid having a higher melting point and weaker acidity than MA (Table S3, Supporting Information), the final carbon exhibits almost identical yield and porosity to MC800 (**Figure 5**a,b). This is most likely influenced by ongoing isomerization reactions during the process, effectively generating the same active species as with MA. When the double bond is replaced by a single bond, as seen in succinic acid, the yield is much lower (10%), even though the number of carbon atoms in the molecule remains the same. At the same time, the SSA remains high (2710 m^2 g^{-1}) but the pores are, on average, 1 nm larger, and thus a higher contribution of mesopores is observed. Subtracting one —COOH, like in the case of acrylic acid, also leads to a lower yield (18%) while maintaining a high SSA (2604 m^2 g^{-1}), but with a much lower contribution of mesopores. It appears that minor structural changes in the molecule can significantly alter the reaction pathway and thereby the yield, and more importantly the porosity of the samples. Notably, the selection of acid-cesium salt is equally or even more important. For instance, pyrolysis of MA and CsCl mixture results in a much lower yield (12%) and lower SSA (1019 m^2 g^{-1}) (Figure S17, Supporting Information). This highlights the importance of in situ formation of Cs oxides, which play a crucial role in facilitating the condensation and activation processes.

2.6. Electrochemical Applications of Porous Carbons

To showcase the potential applications of Cs-mediated porous carbons, we fabricated aqueous Zn-ion capacitors, using MC800 with its higher SSA of 3066 m^2 g^{-1} (Figure S18, Supporting Information) and MC600 with its higher oxygen content (13.5 wt%) and better hydrophilicity (Figure S19, Supporting Information) as porous cathodes. We also analyzed commercial active carbon YP-50F as a reference material for comparison. The cyclic voltammetry analysis of MC600 exhibits a nearly rectangular shape with bumps at 10 mV s^{-1} and well retained at 200 mV s^{-1} (**Figures** 6a, S20, Supporting Information). Despite its lower SSA, MC600 shows a larger cyclic voltammetry area than MC800, suggesting its higher capacitance, possibly attributed to its enhanced hydrophilicity and higher functional oxygen content. In galvanostatic charge/discharge measurements, MC600 also presents a higher specific capacity (capacitance) of 252 mAh g^{-1} (equivalent to 567 F g^{-1}) than MC800 (157 mAh g^{-1}, 356 F g^{-1}). Both are however by far superior to the commercial gold standard YP-50F (60 mAh g^{-1}, 135 F g^{-1}) (Figure 6b and Figure S21, Supporting Information). The specific energy at the material level is very high, 204.8 Wh kg^{-1}, that is, it can easily compete with standard faradaic battery cathodes. Even at a high power rate of 10 A g^{-1}, MC600 still delivers a capacity of 64 mAh g^{-1} (144 F g^{-1}), corresponding to a specific energy of 51.2 Wh kg^{-1}. Importantly, MC800 exhibits excellent cycling stability with nearly 100% capacity retention after 100 000 cycles at 10 A g^{-1} (Figure S22, Supporting Information), exceeding all other state-of-art Zn-ion capacitors based on heteroatom-doped carbon materials, MXene, or metal oxides (Figure 6c and Table S6, Supporting Information). Besides, in aprotic Na-ion capacitors, MC800 and MC600 also exhibit high capacities of 147 and 115 mAh g^{-1} (196 and 153 F g^{-1}) and good cycling stability (Figure S23, Supporting Information). This performance is comparable to or even better than other capacitive materials in organic solvents (Table S7, Supporting Information), underlining the large potential of our porous carbons as cathodes in aqueous and non-aqueous energy storage devices.

3. Conclusion

In conclusion, we present a straightforward and scalable strategy for synthesizing porous carbons with both high yields (>20%) and high SSAs (>3000 m^2 g^{-1}) through direct thermal treatment of Cs salts of simple and cheap carboxylic acids. We have unraveled the reaction pathways and provided new mechanistic insights into the "Cs effect" throughout the framework formation and pore development of carbon. The role of Cs species varies at different stages. First, they efficiently promote the condensation of organics by accelerating dehydration; after Cs reduction, they

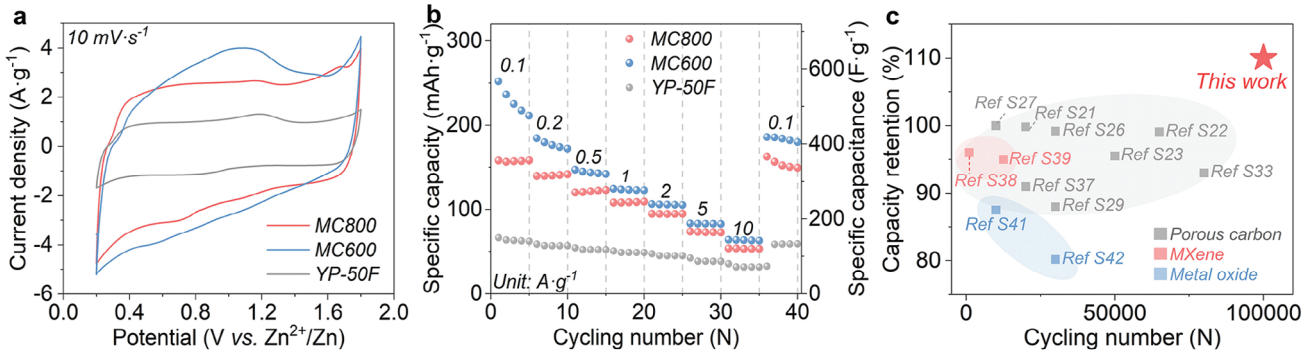

Figure 6. Electrochemical properties of Zn-ion capacitors based on MC800, MC600, or YP-50F as cathodes. a) Cyclic voltammetry curves at 10 mV s^{-1}, b) specific capacities and capacitances at different current densities, and c) cycling performance comparison of Zn-ion capacitors with the reported devices from literature (see citations in Supporting Information).

donate electrons to carbonaceous frameworks, and they intercalate into graphitic layers to form slit nanopores. Cs is practically completely evaporated at the final stage of synthesis via the gas phase and could be recycled from the condensation trap. The resulting porous carbons have demonstrated high capacity and cycling stability as cathodes in both aqueous Zn-ion capacitors and aprotic Na-ion capacitors. The optimal performance of the materials is already obtained at 600 °C, that is, structure formation takes place at a much lower temperature than that of commercial activated carbons (>800 °C). The simplicity of materials and procedures and the easy recovery of Cs salts make the whole process industrially feasible and environmentally sustainable. Overall, our results offer new insights into the unconventional roles of Cs in the conventional synthesis of porous carbons.

Supporting Information

Supporting Information is available from the Wiley Online Library or from the author.

Acknowledgements

The authors gratefully appreciate Katharina ten Brummelhuis for Ar and water sorption measurements, Jessica Brandt for inductively coupled plasma spectroscopy measurements, Eva Settels for MALDI-TOF measurements, Prof. Ke Zeng for mechanism analysis, and the Max Planck Society for financial support. M.O. acknowledges Alexander Von Humboldt Stiftung for financial support. This research received funding from the European Research Council (ERC) under the European Union's Horizon 2020 Research and Innovation Program, MoMa-STOR (grant agreement no. 951513).

Open access funding enabled and organized by Projekt DEAL.

Conflict of Interest

The authors declare no conflict of interest.

Data Availability Statement

The data that support the findings of this study are available from the corresponding author upon reasonable request.

Keywords

activation, cesium effect, molecular precursors, porous carbon, Zn-ion capacitors

Received: November 4, 2023
Revised: December 18, 2023
Published online: January 28, 2024

[1] a) H. Shao, Y. C. Wu, Z. Lin, P. L. Taberna, P. Simon, *Chem. Soc. Rev.* **2020**, *49*, 3005; b) C. O. Ania, P. A. Armstrong, T. J. Bandosz, F. Beguin, A. P. Carvalho, A. Celzard, E. Frackowiak, M. A. Gilarranz, K. László, J. Matos, M. F. R. Pereira, *Carbon* **2020**, *164*, 69; c) W. Tian, H. Zhang, X. Duan, H. Sun, G. Shao, S. Wang, *Adv. Funct. Mater.* **2020**, *30*, 1909265; d) M. Odziomek, P. Giusto, J. Kossmann, N. V. Tarakina, J. Heske, S. M. Rivadeneira, W. Keil, C. Schmidt, S. Mazzanti, O. Savateev, L. Perdigón-Toro, D. Neher, T. D. Kühne, M. Antonietti, N. López-Salas, *Adv. Mater.* **2022**, *34*, 2206405; e) M. Jerigová, M. Odziomek, N. López-Salas, *ACS Omega* **2022**, *7*, 11544; f) F. Béguin, V. Presser, A. Balducci, E. Frackowiak, *Adv. Mater.* **2014**, *26*, 2219; g) D. Hulicova-Jurcakova, M. Seredych, G. Q. Lu, T. J. Bandosz, *Adv. Funct. Mater.* **2009**, *19*, 438.

[2] a) J. Yin, W. Zhang, N. A. Alhebshi, N. Salah, H. N. Alshareef, *Small Methods* **2020**, *4*, 1900853; b) Z. Heidarinejad, M. H. Dehghani, M. Heidari, G. Javedan, I. Ali, M. Sillanpää, *Environ. Chem. Lett.* **2020**, *18*, 393; c) J. Wang, S. Kaskel, *J. Mater. Chem.* **2012**, *22*, 23710.

[3] a) S. Yu, H. Wang, C. Hu, Q. Zhu, N. Qiao, B. Xu, *J. Mater. Chem. A* **2016**, *4*, 16341; b) A. J. Romero-Anaya, M. Ouzzine, M. A. Lillo-Ródenas, A. Linares-Solano, *Carbon* **2014**, *68*, 296; c) X. Liu, M. Antonietti, *Carbon* **2014**, *69*, 460.

[4] a) M. Sevilla, N. Díez, A. B. Fuertes, *ChemSusChem* **2021**, *14*, 94; b) N. Díez, A. B. Fuertes, M. Sevilla, *Energy Storage Mater.* **2021**, *38*, 50; c) M. Sevilla, G. A. Ferrero, A. B. Fuertes, *Carbon* **2017**, *114*, 50; d) J. Pampel, T.-P. Fellinger, *Adv. Energy Mater.* **2016**, *6*, 1502389.

[5] a) Y. Liu, H. Cui, J. Xu, J. Shi, W. Wang, N. Yan, J. Zou, S. You, *Chem. Phys. Lett.* **2023**, *826*, 140655; b) R. Varala, K. S. Rao, *Curr. Org. Chem.* **2015**, *19*, 1242; c) K. Elumeeva, J. Ren, M. Antonietti, T.-P. Fellinger, *ChemElectroChem* **2015**, *2*, 584.

[6] a) G. Yoon, H. Kim, I. Park, K. Kang, *Adv. Energy Mater.* **2017**, *7*, 1601519; b) Y. Liu, B. V. Merinov, W. A. Goddard, *Proc. Natl. Acad. Sci. U. S. A.* **2016**, *113*, 3735;

[7] a) J. Huang, Z. Xu, Y. Yang, *Adv. Funct. Mater.* **2007**, *17*, 1966. b) T. R. Briere, A. H. Sommer, *J. Appl. Phys.* **1977**, *48*, 3547.

[8] a) Z. Liu, H. Wang, *Adv. Electron. Mater.* **2022**, *8*, 2101111; b) T. Li, Y. Rui, X. Wang, J. Shi, Y. Wang, J. Yang, Q. Zhang, *ACS Appl. Energy Mater.* **2021**, *4*, 7002; c) Z. Q. Xu, J. P. Yang, F. Z. Sun, S. T. Lee, Y. Q. Li, J. X. Tang, *Org. Electron.* **2012**, *13*, 697.
[9] a) H. Xu, K. Muto, J. Yamaguchi, C. Zhao, K. Itami, D. G. Musaev, *J. Am. Chem. Soc.* **2014**, *136*, 14834; b) T. Flessner, S. Doye, *J. Prakt. Chem.* **1999**, *341*, 186; c) C. Galli, *Org. Prep. Proced. Int.* **1992**, *24*, 285; d) G. Dijkstra, W. H. Kruizinga, R. M. Kellogg, *J. Org. Chem.* **1987**, *52*, 4230.
[10] a) S. Xu, Z. Liao, A. Dianat, S. Park, M. A. Addicoat, Y. Fu, D. L. Pastoetter, F. G. Fabozzi, Y. Liu, G. Cuniberti, M. Richter, S. Hecht, X. Feng, *Angew. Chem., Int. Ed.* **2022**, *61*, e202202492; b) A. Banerjee, M. W. Kanan, *ACS Cent. Sci.* **2018**, *4*, 606.
[11] I. R. de Larramendi, I. Lozano, M. Enterría, R. Cid, M. Echeverría, S. R. Peña, J. Carrasco, H. Manzano, G. Beobide, I. Landa-Medrano, T. Rojo, N. Ortiz-Vitoriano, *Adv. Energy Mater.* **2022**, *12*, 2102834.
[12] C. Mayeux, L. Massi, J.-F. Gal, L. Charles, P. Burk, *Chem. - Eur. J.* **2014**, *20*, 815.
[13] Y. Nishiyama, Y. Koguma, T. Tanaka, R. Umeda, *Molecules* **2009**, *14*, 3367.
[14] J. Li, J. Kossmann, K. Zeng, K. Zhang, C. Weinberger, M. Antonietti, M. Odziomek, N. López-Salas, *Angew. Chem., Int. Ed.* **2023**, *62*, e202217808.
[15] R. Wojcieszak, F. Santarelli, S. Paul, F. Dumeignil, F. Cavani, R. V. Gonçalves, *Sustainable Chem. Processes* **2015**, *3*, 9.
[16] T. R. Felthouse, J. C. Burnett, B. Horrell, M. J. Mummey, Y. J. Kuo, *Kirk-Othmer Encyclopedia of Chemical Technology*, Wiley, Hoboken, NJ **2006**.
[17] a) X. Y. Zhao, S. S. Huang, J. P. Cao, X. Y. Wei, K. Magarisawa, T. Takarada, *Fuel Process. Technol.* **2014**, *125*, 251; b) Q. Cao, K. C. Xie, Y. K. Lv, W. R. Bao, *Bioresour. Technol.* **2006**, *97*, 110;
[18] a) K. A. Cychosz, R. Guillet-Nicolas, J. García-Martínez, M. Thommes, *Chem. Soc. Rev.* **2017**, *46*, 389; b) M. Thommes, K. Kaneko, A. V. Neimark, J. P. Olivier, F. Rodriguez-Reinoso, J. Rouquerol, K. S. W. Sing, *Pure Appl. Chem.* **2015**, *87*, 1051.
[19] a) G. Singh, J. Lee, A. Karakoti, R. Bahadur, J. Yi, D. Zhao, K. Albahily, A. Vinu, *Chem. Soc. Rev.* **2020**, *49*, 4360; b) A. C. Dassanayake, M. Jaroniec, *J. Mater. Chem. A* **2017**, *5*, 7955; c) J. Zhou, Z. Li, W. Xing, H. Shen, X. Bi, T. Zhu, Z. Qiu, S. Zhuo, *Adv. Funct. Mater.* **2016**, *26*, 7955.
[20] a) J. Li, L. Wang, Y. Zhao, S. Li, X. Fu, B. Wang, H. Peng, *Adv. Funct. Mater.* **2020**, *30*, 2001619; b) X. Li, J. Zhou, J. Zhang, M. Li, X. Bi, T. Liu, T. He, J. Cheng, F. Zhang, Y. Li, X. Mu, J. Lu, B. Wang, *Adv. Mater.* **2019**, *31*, 1903852.
[21] a) S. Khodabakhshi, M. Taddei, J. A. Rudd, M. J. McPherson, Y. Niu, R. E. Palmer, A. R. Barron, E. Andreoli, *Carbon* **2021**, *173*, 989; b) Z. Zhang, Z. P. Cano, D. Luo, H. Dou, A. Yu, Z. Chen, *J. Mater. Chem. A* **2019**, *7*, 20985.
[22] a) Y. Liu, J. Wilcox, *Environ. Sci. Technol.* **2012**, *46*, 1940; b) Y. Liu, J. Wilcox, *Int. J. Coal Geol.* **2012**, *104*, 83; c) X. Ma, L. Li, R. Chen, C. Wang, H. Li, S. Wang, *Appl. Surf. Sci.* **2018**, *435*, 494; d) B. Ashourirad, P. Arab, T. Islamoglu, K. A. Cychosz, M. Thommes, H. M. El-Kaderi, *J. Mater. Chem. A* **2016**, *4*, 14693; e) M. Saleh Shafeeyan, W. Mohd Ashri Wan Daud, A. Houshmand, A. Shamiri, *J. Anal. Appl. Pyrolysis* **2010**, *89*, 143.
[23] Y. Zhu, S. Murali, M. D. Stoller, K. J. Ganesh, W. Cai, P. J. Ferreira, A. Pirkle, R. M. Wallace, K. A. Cychosz, M. Thommes, D. Su, E. A. Stach, R. S. Ruoff, *Science* **2011**, *332*, 1537.
[24] D. B. Schuepfer, F. Badaczewski, J. M. Guerra-Castro, D. M. Hofmann, C. Heiliger, B. Smarsly, P. J. Klar, *Carbon* **2020**, *161*, 359.
[25] A. Band, A. Albu-Yaron, T. Livneh, H. Cohen, Y. Feldman, L. Shimon, R. Popovitz-Biro, V. Lyahovitskaya, R. Tenne, *J. Phys. Chem. B* **2004**, *108*, 12360.
[26] a) A. Valor, E. Reguera, E. Torres-García, S. Mendoza, F. Sanchez-Sinencio, *Thermochim. Acta* **2002**, *389*, 133; b) J. Mu, D. D. Perlmutter, *Thermochim. Acta* **1981**, *49*, 207; c) K. C. Patil, G. V. Chandrashekhar, M. V. George, C. N. R. Rao, *Can. J. Chem.* **1968**, *46*, 257.
[27] a) C. Guéneau, J.-L. Flèche, *Calphad* **2015**, *49*, 67; b) H. Okamoto, *J. Phase Equilib. Diffus.* **2010**, *31*, 86.
[28] a) W. Klemm, H.-J. Scharf, *Z. Anorg. Allg. Chem.* **1960**, *303*, 263; b) Y. Li, D. Zhang, L. Duan, R. Zhang, L. Wang, Y. Qiu, *Appl. Phys. Lett.* **2007**, *90*, 012119.
[29] J. Zhao, Y. Cai, J. P. Yang, H. X. Wei, Y. H. Deng, Y. Q. Li, S. T. Lee, J. X. Tang, *Appl. Phys. Lett.* **2012**, *101*, 193303.
[30] H. G. Limberger, T. P. Martin, *Z. Phys. D: At., Mol. Clusters* **1989**, *12*, 439.
[31] M. Petrović, I. Šrut Rakić, S. Runte, C. Busse, J. T. Sadowski, P. Lazić, I. Pletikosić, Z. H. Pan, M. Milun, P. Pervan, N. Atodiresei, R. Brako, D. Šokčević, T. Valla, T. Michely, M. Kralj, *Nat. Commun.* **2013**, *4*, 2772.
[32] a) W. Li, S. Lin, N. T. T. Tran, M. Lin, K. Lin, *RSC Adv.* **2020**, *10*, 23573; b) U. Mizutani, T. Kondow, T. B. Massalski, *Phys. Rev. B* **1978**, *17*, 3165.
[33] a) R. Matsumot, N. Akuzawa, Y. Takahashi, *Mater. Trans.* **2006**, *47*, 1458; b) J. E. Fischer, T. E. Thompson, *Phys. Today* **1978**, *31*, 36.
[34] F. Pan, K. Ni, Y. Ma, H. Wu, X. Tang, J. Xiong, Y. Yang, C. Ye, H. Yuan, M. L. Lin, J. Dai, M. Zhu, P. H. Tan, Y. Zhu, K. S. Novoselov, *Nano Lett.* **2021**, *21*, 5648.
[35] a) F. Pan, K. Ni, T. Xu, H. Chen, Y. Wang, K. Gong, C. Liu, X. Li, M. L. Lin, S. Li, X. Wang, W. Yan, W. Yin, P. H. Tan, L. Sun, D. Yu, R. S. Ruoff, Y. Zhu, *Nature* **2023**, *614*, 95; b) A. Etxebarria, S. L. Koch, O. Bondarchuk, S. Passerini, G. Teobaldi, M. Á. Muñoz-Márquez, *Adv. Energy Mater.* **2020**, *10*, 2000520; c) K. Xie, L. Duan, D. Zhang, J. Qiao, G. Dong, L. Wang, Y. Qiu, *J. Phys. D: Appl. Phys.* **2010**, *43*, 252001.
[36] H. L. Skriver, N. M. Rosengaard, *Phys. Rev. B* **1992**, *46*, 7157.
[37] a) E. Raymundo-Piñero, P. Azaïs, T. Cacciaguerra, D. Cazorla-Amorós, A. Linares-Solano, F. Béguin, *Carbon* **2005**, *43*, 786; b) R. Xue, Z. Shen, *Carbon* **2003**, *41*, 1862.
[38] a) L. Zhu, Y. Li, J. Zhang, X. Gan, Q. Li, T. Tang, Y. Chen, J. Zhu, N. Guo, L. Wang, S. Zhang, *Appl. Surf. Sci.* **2023**, *638*, 158051; b) H. J. Lee, D. Ko, J. Kim, Y. Park, I. Hwang, C. T. Yavuz, J. W. Choi, *ChemNanoMat* **2021**, *7*, 150.
[39] S. Kundu, Y. Wang, W. Xia, M. Muhler, *J. Phys. Chem. C* **2008**, *112*, 16869.